Mechanistic Modeling of *Porphyridium* sp. Growth under Photoperiod Variation Using a Droop–Steele Dynamical System

Rifky Fauzi[1,*], Yoga Andriyanto[1], Nela Rizka[1], Tiara Shofi Edriani[1], Aswan Anggun Pribadi[1], Ciptaning Weargo Jati[2] & Dear Michiko Mutiara Noor[1]

[1]Department of Mathematics, Faculty of Science, Institut Teknologi Sumatera, Lampung Selatan, 35365, Indonesia
[2]Department of Aquaculture, Faculty of Agriculture, University of Lampung, Bandar Lampung, 35141, Indonesia
*E-mail: rifky.fauzi@ma.itera.ac.id

Abstract. Longer illumination can increase *Porphyridium* sp. biomass but requires more energy. We studied growth under 6 h, 12 h, and 24 h photoperiods using a Droop–Steele dynamical model for external nutrient N, internal quota Q, and cell density X. Photoperiod modifies nutrient uptake through a daily-effective Steele factor. We established forward invariance of the biologically feasible region and ultimate boundedness, derived washout and positive-biomass equilibria, and characterized local stability. Parameters were estimated jointly from 81 container-day observations across nine independent cultures using Bayesian inference. Four Markov chain Monte Carlo chains met the reported convergence criteria (maximum $\hat{R} = 1.0032$). Posterior draws were mapped onto analytical persistence and stability conditions and propagated to biomass predictions. All tested photoperiods yielded a feasible, locally stable positive equilibrium within the fitted model. Predicted biomass increased with illumination but showed diminishing gains per additional lighting hour. The fitted effective-light Steele response was nearly linear over the tested range; the modeled flattening was consistent with nutrient depletion and quota limitation without requiring photoinhibition. Droop–Steele had the lowest AICc among the models compared, although Logistic had marginally lower raw log-RMSE. Energy-use and cost data are needed before identifying a cost-optimal photoperiod.

Keywords: *Bayesian parameter estimation; Droop–Steele model; photoperiod;* Porphyridium *sp.; stability.*

1 Introduction

Porphyridium sp. is a unicellular red microalga used as natural feed in aquaculture and as a source of pigments, polysaccharides, and other bioactive compounds [1, 2, 3, 4]. Understanding its growth is therefore important both for

Received May 4th, 2026, Revised August 25th, 2026, Accepted for publication September 2nd, 2026
Copyright © 2026 Published by ITB Institute for Research and Community Service, ISSN: 2337-5760, DOI: 10.5614/j.math.fund.sci.2026.58.1.4

culture performance and for day-to-day operation. Biomass and bioproduct yields depend on several conditions, including irradiance, nitrogen availability, salinity, cultivation strategy, and light/dark scheduling [5, 6, 7, 8, 9]. Photoperiod is especially convenient to adjust in indoor LED cultures. More hours of light, however, do not necessarily give a proportional increase in biomass. Empirical growth curves describe changes in cell density, but they give little insight into how nutrients move from the surrounding medium into the cells and eventually contribute to growth. The Droop model addresses this distinction by relating growth to intracellular nutrient quota rather than directly to the nutrient concentration in the medium [10, 11]. Quota-based models remain relevant to studies of parameter identification, periodically varying light and global dynamics [12, 13, 14]. Without direct measurements inside the cells, however, quota should be interpreted as an effective physiological variable rather than a separately verified intracellular quantity [15]. Light and nutrient limitations can be linked through the nutrient-uptake process [16].

Here, we consider LED photoperiods of 6 h, 12 h, and 24 h. Beyond asking which treatment produces more cells, we ask whether changing the lighting duration moves the culture between washout and persistence or simply changes biomass within a common persistence regime. An explicit mechanistic threshold helps answer this question: unlike a fitted carrying capacity, it identifies the balance between nutrient uptake and the quota required to maintain biomass.

Our contribution lies in bringing established components together and testing what their combination reveals about these experiments; we do not claim that the Droop, Monod, or Steele laws, stability methods, or Bayesian inference are individually new. We incorporate photoperiod into nutrient uptake through Steele's response, then derive a washout–persistence margin and relate it to the dominant eigenvalue at washout. We establish positivity and ultimate boundedness and examine convergence numerically over a range of initial conditions. Finally, we apply the analytical conditions to Bayesian posterior draws, propagate parameter uncertainty to biomass predictions, and compare Droop–Steele with Logistic and Monod models fitted to the same observations.

2 Model Assumptions and Formulation

We treat the culture as a single, well-mixed population. The available observations are culture-level cell densities, so the model does not resolve cell-size differences, variation in quota between individual cells, spatial nutrient gradients, or light attenuation. These features can be considered when physiological or spatial data are available [17, 18]. Cell density serves as a proxy for biomass, and one effective limiting nutrient represents nutrient availability.

Effects of other controlled culture conditions are incorporated into effective parameters. This keeps the model at a level of detail that the observations can reasonably support.

The causal mechanism is:

photoperiod → light-dependent uptake → internal quota → biomass growth (1)

Here, photoperiod is an experimental input, while $N(t)$, $Q(t)$, and $X(t)$ evolve over time. Figure 1 illustrates their roles and the direction of the proposed mechanism.

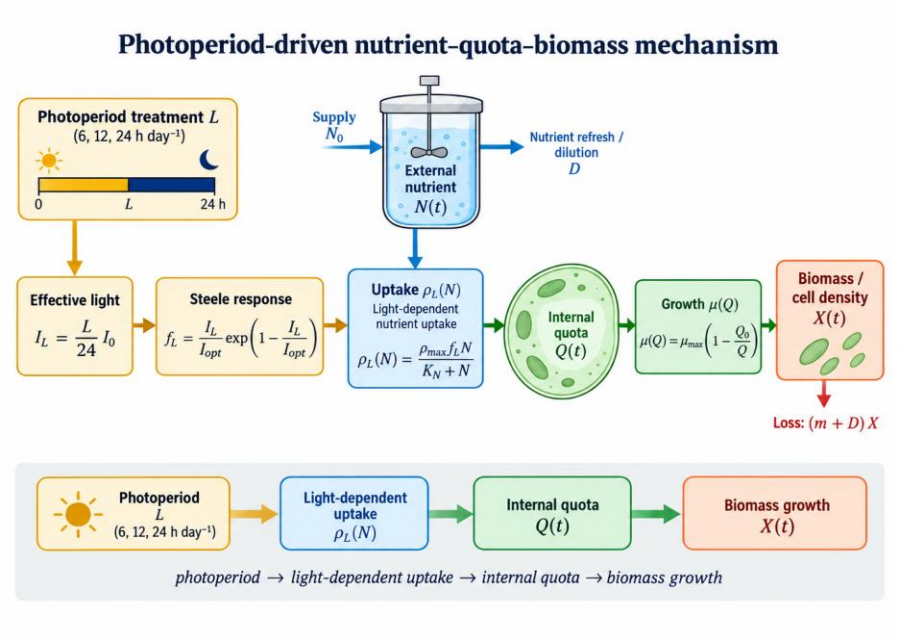


Figure 1 Mechanistic structure of the Droop–Steele model. The photoperiod treatment L determines the daily-effective light response, which modifies nutrient uptake $\rho_L(N)$. Uptake links external nutrient $N(t)$ to internal quota $Q(t)$ and quota-dependent growth $\mu(Q)$ determines biomass $X(t)$.

For a fixed photoperiod L, the governing autonomous system is

$$\frac{dN}{dt} = D(N_0 - N) - \rho_L(N)X, \tag{2}$$

$$\frac{dX}{dt} = \big(\mu(Q) - (m + D)\big)X, \tag{3}$$

$$\frac{\mathrm{d}Q}{\mathrm{d}t} = \rho_L(N) - \mu(Q)Q. \tag{4}$$

The quota-dependent growth law is the Droop form [10, 11],

$$\mu(Q) = \mu_{\max}\left(1 - \frac{Q_0}{Q}\right), \qquad Q > Q_0. \tag{5}$$

The nutrient-saturation factor in uptake follows a Monod-type structure [19, 20], while the present study multiplies that saturation by the photoperiod response,

$$\rho_L(N) = \rho_{\max} f_L \frac{N}{K_N + N}. \tag{6}$$

The light factor adopts Steele's photosynthesis–irradiance response [21], with photoperiod represented by an effective light index rather than directly measured instantaneous irradiance,

$$f_L = \frac{I_L}{I_{\mathrm{opt}}}\exp\left(1 - \frac{I_L}{I_{\mathrm{opt}}}\right), \qquad I_L = \frac{L}{24} I_0. \tag{7}$$

Equations (2)–(4) combine these established growth, uptake, and light-response laws. Physiological parameters are shared between treatments, changing $L \in \{6,12,24\}$ h changes only f_L. Steele's response reaches an optimum at $I_L/I_{\mathrm{opt}} = 1$ and decreases beyond it. Because instantaneous irradiance was not measured independently, any conclusion about the light-response regime is conditional on the effective-light representation used here. The state variables and model parameters are summarized in Table 1.

Table 1 State variables and parameters in the Droop–Steele system.

Symbol	Type	Unit	Interpretation
t	independent variable	day	culture time
N	state variable	nutrient unit	external limiting nutrient
X	state variable	10^6 cells ml^{-1}	biomass proxy or cell density
Q	state variable	nutrient per biomass	internal nutrient quota
D	parameter	day^{-1}	effective nutrient refresh or dilution rate
N_0	parameter	same as N	reference external nutrient level
m	parameter	day^{-1}	biomass loss or maintenance rate

Symbol	Type	Unit	Interpretation
$\mu_{\max}$	parameter	day^{-1}	maximum specific growth rate
Q_0	parameter	same as Q	subsistence quota
$\rho_{\max}$	parameter	quota day^{-1}	maximum uptake scale
K_N	parameter	same as N	half-saturation nutrient level
I_0 /I_{opt}	parameter	dimensionless	effective lamp-to-optimal irradiance ratio
L	treatment	h day^{-1}	photoperiod duration

3 Positivity, Boundedness, Equilibria, and Persistence Threshold

The biologically feasible region is

$$\Omega = \{(N, X, Q): 0 \le N \le N_0,\ X \ge 0,\ Q \ge Q_0\}. \tag{8}$$

Proposition 1. If $\big(N(0), X(0), Q(0)\big) \in \Omega$, the solution of Eqs. (2) – (4) remains in Ω for all $t \ge 0$.

Proof. At $N = 0$, $\rho_L(0) = 0$, so $\dot{N} = DN_0 > 0$. At $N = N_0$, $\dot{N} = -\rho_L(N_0)X \le 0$. At $X = 0$, $\dot{X} = 0$. At $Q = Q_0$, $\mu(Q_0) = 0$, so $\dot{Q} = \rho_L(N) \ge 0$. Hence, the vector field does not point out of Ω. ▫

The nutrient boundary has another implication. When $D > 0$ and $N_0 > 0$, nutrient concentration cannot remain at zero because $\dot{N}|_{N=0} = DN_0 > 0$: the refresh term returns the system to positive nutrient levels. Concentration may become very small, however. In a closed-batch model with $D = 0$, this argument no longer applies.

The local positivity argument can be strengthened with a global boundedness estimate. Define

$$V(N, X, Q) = N + QX. \tag{9}$$

Using Eqs. (2) – (4), cancellation of the uptake and quota-conversion terms gives

$$\dot{V} = D(N_0 - N) - (m + D)QX. \tag{10}$$

Let $k = \min\{D, m + D\} > 0$. Then

$$\dot{V} \le DN_0 - kV. \tag{11}$$

It follows that $V(t) \le V(0)e^{-kt} + DN_0\left(1 - e^{-kt}\right)/k$ and limsup (t→∞) $V(t) \le DN_0/k$. Since $0 \le N(t) \le N_0$ and ρ_L is increasing, the quota equation also gives $\dot{Q} \le \rho_L(N_0) - \mu_{\max}(Q - Q_0)$; comparison therefore yields limsup (t→∞) $Q(t) \le Q_0 + ho_L(N_0)/\mu_{\max}$. Finally, $X(t) \le V(t)/Q_0$ for $Q_0 > 0$. Thus N, X, and Q are all ultimately bounded.

Let $a = m + D$. Setting the three right-hand sides of Eqs. (2)–(4) equal to zero gives two biologically relevant equilibrium branches. The zero-biomass (washout) equilibrium is

$$E_0 = \left(N_0,\ 0,\ Q_0 + \frac{\rho_L(N_0)}{\mu_{\max}}\right). \tag{12}$$

The washout state E_0 is therefore not the origin $(0,0,0)$. Biomass vanishes, but the external nutrient and the quota coordinate remain positive.

For a positive-biomass equilibrium, $X^* > 0$ requires $\mu(Q^*) = a$. Therefore

$$Q^* = \frac{\mu_{\max} Q_0}{\mu_{\max} - a}, \qquad R^* = aQ^*, \qquad \mu_{\max} > a. \tag{13}$$

The positive equilibrium can then be written explicitly as

$$E_+ = (N^*, X^*, Q^*) = \left(\frac{K_N R^*}{\rho_{\max} f_L - R^*},\ \frac{D}{R^*}\left[N_0 - \frac{K_N R^*}{\rho_{\max} f_L - R^*}\right],\ \frac{\mu_{\max} Q_0}{\mu_{\max} - a}\right). \tag{14}$$

It is a biologically positive equilibrium, with $N^* > 0$, $X^* > 0$, and $Q^* > Q_0$, whenever

$$\mu_{\max} > a, \qquad \rho_L(N_0) > R^*. \tag{15}$$

We therefore define the photoperiod-dependent persistence margin

$$\Delta_L = \rho_L(N_0) - R^*. \tag{16}$$

The sign of Δ_L indicates whether the culture can maintain positive biomass. A negative margin means that light-dependent uptake at the available nutrient level falls short of the quota demand associated with biomass losses. A positive margin permits a positive-biomass equilibrium.

4 Local Stability and Stability-Exchange Threshold

Let

$$s(N) = \rho_L{}'(N) = \rho_{\max} f_L \frac{K_N}{(K_N + N)^2}, \qquad h(Q) = \mu'(Q) = \mu_{\max} \frac{Q_0}{Q^2}. \quad (17)$$

The Jacobian is

$$J(N, X, Q) = \begin{pmatrix} -D - s(N)X & -\rho_L(N) & 0 \\ 0 & \mu(Q) - a & h(Q)X \\ s(N) & 0 & -h(Q)Q - \mu(Q) \end{pmatrix}. \quad (18)$$

At E_0, two eigenvalues are strictly negative, and the biomass-direction eigenvalue is $\lambda_b = \mu(Q_w) - a$, where $Q_w = Q_0 + \rho_L(N_0)/\mu_{\max}$. Substituting Q_w into the Droop growth function gives the equivalent expression

$$\lambda_b(E_0) = \frac{(\mu_{\max} - a)\Delta_L}{\mu_{\max} Q_0 + \rho_L(N_0)}. \quad (19)$$

Provided $\mu_{\max} > a$, λ_b and Δ_L have the same sign. Washout is locally asymptotically stable when $\Delta_L < 0$ and unstable to biomass perturbations when $\Delta_L > 0$. The condition that allows a positive-biomass equilibrium is therefore also the condition at which washout changes local stability.

At the boundary $\Delta_L = 0$, $N^* \to N_0$, $X^* \to 0$, and $Q^* \to Q_w$, so the positive and zero-biomass branches meet while $\lambda_b = 0$. The continuation therefore identifies the transition in local stability at the biomass-maintenance threshold.

At E_+, $\mu(Q^*) = a$ and $\rho_L(N^*) = R^*$. Define

$$A = D + s(N^*)X^*, \qquad M = h(Q^*)Q^* + a, \qquad B = R^* h(Q^*) X^* s(N^*). \quad (20)$$

The characteristic polynomial is

$$p(\lambda) = \lambda^3 + c_1\lambda^2 + c_2\lambda + c_3, \quad (21)$$

with $c_1 = A + M$, $c_2 = AM$, and $c_3 = B$. All coefficients are positive at a feasible E_+. By the cubic Routh–Hurwitz criterion, E_+ is locally asymptotically stable if

$$c_1 c_2 > c_3. \quad (22)$$

The condition compares the damping associated with nutrient recovery and quota relaxation with the feedback between uptake, quota, and biomass. When the former dominates in the sense of Eq. (22), the positive equilibrium is locally asymptotically stable.

5 Numerical Stability Evidence and Robustness

We first examine the stability results numerically using the reference parameters in Table 2, independently of fitting the experimental data. Parameters chosen solely for this exercise are labeled as assumed; literature references support the model forms rather than those numerical values. The reference set is used to examine the threshold, local stability, and responses to finite perturbations.

Table 2 Reference parameter set for the numerical stability analysis.

Parameter	Value	Reference
D	0.05	Assumed reference value; the chemostat-type nutrient-refresh structure follows [22].
m	0.02	Assumed biomass-loss rate for the numerical stability analysis.
$\mu_{\max}$	1.00	Assumed maximum growth rate satisfying $\mu_{\max} > m + D$.
Q_0	0.20	Assumed subsistence-quota scale; the quota-growth formulation follows Droop [10, 11].
$\rho_{\max}$	0.60	Assumed maximum uptake scale for the numerical stability analysis.
K_N	0.20	Assumed half-saturation value; the nutrient-saturation structure follows Monod [19].
N_0	1.00	Assumed normalized external-nutrient reference.
I_0/I_{opt}	1.00	Reference value corresponding to the Steele optimum; the light-response function follows [21].

For this reference set, the washout–persistence threshold is $L_{\mathrm{crit}} = 0.269$ h day^{-1}. Figure 2 follows the equilibrium branches and the dominant eigenvalue through the threshold. All three experimental treatments (6 h, 12 h, and 24 h) fall on the positive-biomass side of this reference calculation.

Figure 3 shows trajectories starting from finite perturbations around E_0 and E_+. Open circles indicate starting points and triangles indicate final states. To assess a wider set of starting states, we also integrated 100 positive initial conditions per photoperiod for 180 days. Median final relative distances to E_+ were 6.35×10^{-6}, 6.15×10^{-6}, and 7.36×10^{-6} at 6 h, 12 h, and 24 h, respectively; all maximum distances were below 2.72×10^{-5}. These results describe the tested numerical basin and do not constitute a proof of global stability.

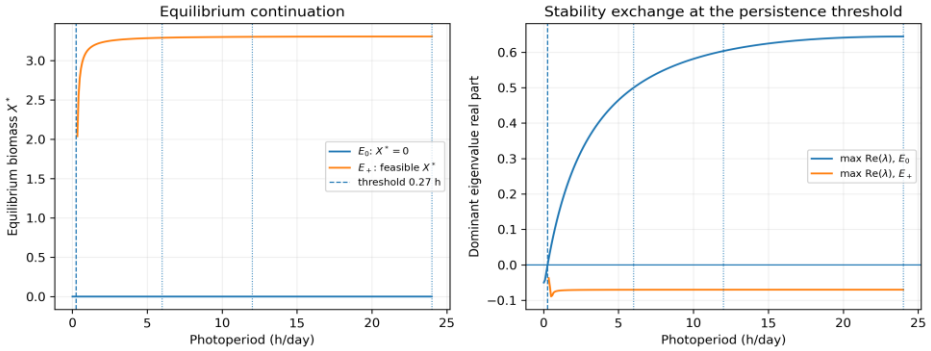


Figure 2 Equilibrium continuation and dominant-eigenvalue tracking versus photoperiod for the reference parameter set. The equilibrium branches meet and the dominant eigenvalue crosses zero at the biomass-maintenance threshold.

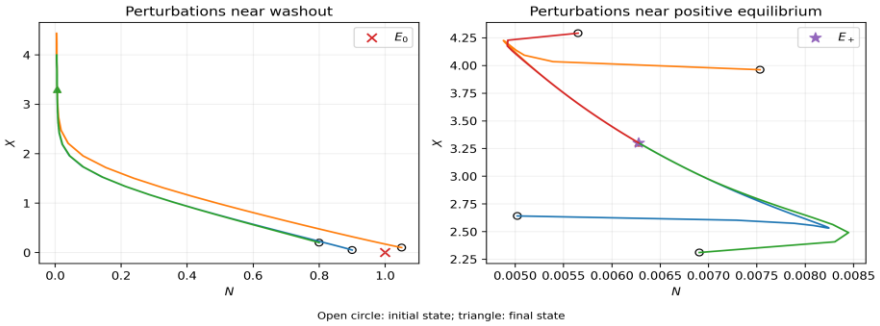


Figure 3 Finite perturbations near the zero-biomass equilibrium (left) and positive equilibrium (right) for the 12 h scenario. Open circles denote initial states, triangles denote final states, and the equilibrium locations are marked by E_0 and E_+, respectively.

For Figure 4, we ran three separate simulations with L fixed at 6 h, 12 h, or 24 h throughout each run. The lamp was not switched on and off within each simulated day. Instead, each treatment entered the model through its constant daily effective Steele factor f_L. The curves therefore compare treatment-level changes in external nutrient, quota, and biomass, not within-day light/dark dynamics.

We also checked how sensitive persistence is to the chosen reference parameters. In 3,000 parameter sets, each entry in Table 2 was independently multiplied by a log-uniform factor between 0.5 and 1.5. Persistence occurred in 100% of the sampled sets at each of the three photoperiods. Median margins were 0.185, 0.303, and 0.388, with corresponding 5–95% ranges of 0.086–0.378, 0.158–

0.567, and 0.229–0.665. This is a robustness check over a specified perturbation range, not an estimate of parameter uncertainty from the data.

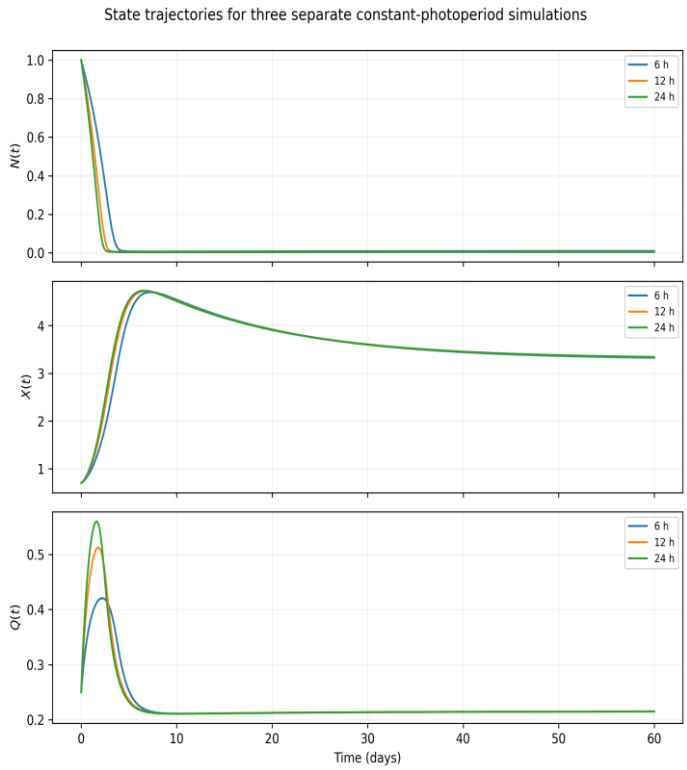


Figure 4 External nutrient, biomass, and internal quota trajectories from three separate simulations with $L = 6$, 12, or 24 h day^{-1}. Each value of L remains fixed throughout its simulation through the daily-effective light factor; within-day light/dark switching is not modeled explicitly.

6 Experimental Data and Bayesian Parameter Estimation

The experiment included three photoperiods (6 h, 12 h, and 24 h), with three independent culture containers for each treatment. Each container was observed on nine days, and three microscopic counts were taken at each observation. We averaged the technical counts within each container on each day, yielding 81 container-day measurements from nine independent cultures. The 81 measurements are repeated observations, not 81 independent biological replicates. Figure 5 presents treatment means and standard deviations across the three container means on each observation day.

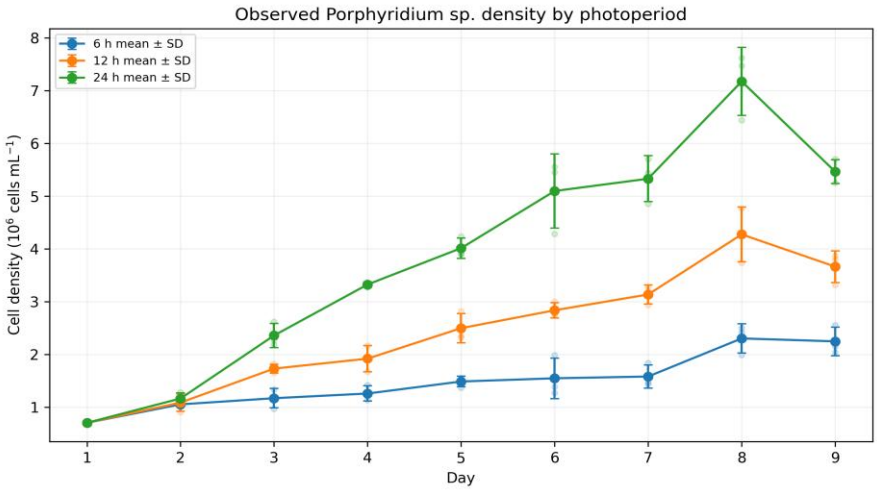


Figure 5 Observed *Porphyridium* sp. density by photoperiod. Markers/bars summarize treatment means and error bars represent standard deviations across three independent culture-container means.

We set $t = 0$ at the first observation. Experimental days $i = 1, \ldots, 9$ therefore correspond to model times $t_i = i - 1$; no unobserved period was simulated before the first measurement. Each treatment started from $N(0) = N_0$, $X(0) = 0.7$ (in 10^6 cells ml^{-1}), and $Q(0) = Q_{\text{init}}$, with the initial quota estimated from the data.

The model was fit jointly to all 81 container-day observations. The positive cell-density observations were modeled using Gaussian errors on the log scale and assumed conditional independence given the model parameters. This is a working likelihood assumption, as repeated observations from the same container may be temporally correlated.

$$\log Y_{\ell w}(t_i) \mid \theta, \sigma_{\log} \sim \mathcal{N}\left(\log X_{\ell}(t_i; \theta), \sigma_{\log}^2\right), \tag{23}$$

where $\ell \in \{6,12,24\}$ h denotes photoperiod, $w = 1,2,3$ denotes culture container, and $i = 1, \ldots, 9$ denotes observation day. The structural parameters estimated jointly were

$$\theta = \left(\mu_{\max}, \rho_{\max}, N_0, I_0/I_{\text{opt}}, Q(0)\right),$$

while $Q_0 = 0.03$, $K_N = 0.30$, $m = 0.02$, and $D = 0.02$ were held fixed because biomass-only observations do not support stable simultaneous identification of all physiological quantities.

Let

$$r_{\ell wi}(\theta) = \log Y_{\ell w}(t_i) - \log X_\ell(t_i;\theta).$$

For $n = 81$ observations, the log-likelihood evaluated at every proposed parameter vector is

$$\ell\big(\theta, \sigma_{\log}; Y\big) = -\frac{n}{2}\log(2\pi) - n\log\sigma_{\log} - \frac{1}{2\sigma_{\log}^2}\sum_{\ell}\sum_{w}\sum_{i} r_{\ell wi}\,(\theta)^2. \quad (24)$$

Equation (24) connects the differential-equation model to the observations. For each proposed parameter set, we solved for $X_\ell(t_i;\theta)$ and compared its log values with the measured densities. Smaller discrepancies give a larger likelihood. The Gaussian observation model follows Bayesian approaches used for microbial and bioprocess growth [23, 24]. Algorithm 1 follows the general organization of the computational estimation workflow of Puspita et al. [25], while the observation model was motivated by the bioprocess literature cited above.

Positive parameters are represented on the log scale and assigned independent weakly informative Gaussian priors. Let

$$\phi \;=\; (\mu_{max}, \rho_{max}, N_0, \frac{I_0}{I_{opt}}, Q(0), \sigma_{log}).$$

For $z_j \;=\; log\;\phi_j$, the prior specification was

$$z_j \;\sim\; \mathrm{N}(log\;c_j, {s_j}^2),\;\; j \;=\; 1, \ldots, 6.$$

The corresponding prior centers and log-scale standard deviations were

$$c \;=\; (3.5, 1.0, 0.17, 0.03, 0.043, 0.15),$$
$$s \;=\; (0.75, 1.20, 0.70, 1.10, 0.40, 0.65).$$

The priors were truncated to the following finite ranges:

$$0.05 \;<\; \mu_{max} \;<\; 20,\;\; 0.005 \;<\; \rho_{max} \;<\; 50,\;\; 0.005 \;<\; N_0 \;<\; 5,$$
$$10^{-4} \;<\; \frac{I_0}{I_{opt}} \;<\; 5,\;\; Q_0 \;<\; Q(0) \;<\; 1,\;\; 0.01 \;<\; \sigma_{log} \;<\; 1.$$

These bounds were imposed for biological and numerical admissibility. The sampling target is the posterior density,

$$\pi\big(\theta, \sigma_{\log} \mid Y\big) \propto \exp\{\ell\big(\theta, \sigma_{\log}; Y\big)\}\, p(\theta)\, p\big(\sigma_{\log}\big). \quad (25)$$

Rather than stopping at the parameter vector that maximizes the likelihood, we sampled from the posterior in Eq. (25). This distribution combines the information in the observations with the prior distributions and allows parameter uncertainty to be carried into subsequent calculations.

Algorithm 1. Bayesian Parameter Estimation for the Droop–Steele ODE
Input: Container-level observations $Y_{\ell w}(t_i)$ for $\ell = 6{,}12{,}24$ h and prior distributions for the estimated parameters.
Data: Droop–Steele ODEs in Eqs. (2)–(4); fixed parameters Q_0, K_N, m, D; observation model in Eq. (23).
Output: Posterior samples of θ and $\sigma_{\log}$, convergence diagnostics, and post-estimation evaluation of the analytical existence and stability conditions.

1. Compute a posterior-mode estimate in log-parameter space and a local covariance approximation
2. Initialize four independent Markov chains around the posterior mode
3. For each chain, do the following
4. For each Metropolis–Hastings iteration, do the following
5. Draw a positive-parameter proposal in log space
6. Solve Eqs. (2)–(4) for $L = 6{,}12{,}24$ h at the observation times
7. Evaluate the log-likelihood in Eq. (24) and the log-posterior in Eq. (25)
8. Accept or reject the proposal using the Metropolis–Hastings probability
9. Discard burn-in iterations and retain posterior draws
10. Compute rank-normalized split-$\hat{R}$ and bulk effective sample size (ESS)
11. For each retained posterior draw, do the following
12. Evaluate Eqs. (15), (16), and (22)

Table 3 Bayesian parameter-estimation summary from the 81 container-day observations. Intervals are 5th–95th posterior quantiles.

Parameter	5%	Median	95%
$\mu_{\max}$	2.575	3.645	5.532
$\rho_{\max}$	0.250	0.778	2.906
N_0	0.1602	0.1732	0.1896
I_0/I_{opt}	0.00679	0.02578	0.07937
$Q(0)$	0.03916	0.04217	0.04573
$\sigma_{\log}$	0.1122	0.1263	0.1453

To keep repeated likelihood evaluations computationally manageable, we integrated the ODEs with a fixed-step fourth-order Runge–Kutta method (RK4), using a step of 0.02 day. We checked this implementation against LSODA, an

adaptive integrator that switches between nonstiff and stiff formulas. At the initialization point, the maximum biomass difference over the nine observation days was below 2×10^{-7}. Each of four Metropolis–Hastings chains used 250 burn-in iterations followed by 1,200 retained draws. The largest rank-normalized split-$\hat{R}$ was 1.0032 and the smallest bulk effective sample size (ESS) was 838, meeting the prespecified limits of $\hat{R} \leq 1.01$ and $\mathrm{ESS} \geq 400$. Equilibrium existence and stability were assessed after sampling; neither condition was imposed in the likelihood or acceptance step.

The posterior median of $\mu_{\max}$ is 3.645 day^{-1}, higher than specific growth rates commonly measured directly in *Porphyridium* cultures. This parameter, however, is the asymptotic maximum of the Droop growth law, not the rate necessarily realized by a culture with limited quota. At the median initial quota $Q(0) = 0.04217$, Eq. (5) gives $\mu\big(Q(0)\big) = 1.052$ day^{-1}, or approximately 1.012 day^{-1} after subtracting $m + D$. Oh et al. [26] reported 0.042 h^{-1} (1.008 day^{-1}) for *P. cruentum* under an 18:6 h light:dark cycle. The realized rate is therefore of a comparable order of magnitude. We nevertheless interpret the latent maximum cautiously: biomass observations alone offer limited information for distinguishing growth capacity from quota dynamics.

The posterior correlation between $\rho_{\max}$ and I_0/I_{opt} is -0.611. Higher values of one parameter can partly compensate for lower values of the other, making their separate interpretation uncertain. The biomass observations constrain the combined uptake function $\rho_L(N)$ more directly than either parameter on its own.

7 Posterior Regime Mapping and Uncertainty Propagation

We next applied the analytical conditions to the retained posterior draws. For each draw, we calculated the persistence margin in Eq. (16), allowing us to estimate

$$\mathbb{P}(\Delta_L > 0 \mid \text{data}), \tag{26}$$

At every tested photoperiod, the posterior proportion of draws satisfying persistence was 1.000; the same proportion satisfies local stability of the feasible positive equilibrium. Median persistence margins rose from 0.00375 (5–95%: 0.00330–0.00425) at 6 h to 0.00861 (0.00775–0.00962) at 12 h and 0.01813 (0.01633–0.02020) at 24 h. Thus, all three treatments fall in the same persistence regime, but longer photoperiods place the fitted system farther from the washout threshold.

Figure 6 connects these two uses of the posterior. On the left, trajectories generated from posterior draws are compared with the biomass observations. On the right, those identical draws are evaluated using Δ_L. No additional fitting occurs in the second panel: it simply shows how uncertainty in the fitted parameters translates into uncertainty about the analytically defined persistence threshold.

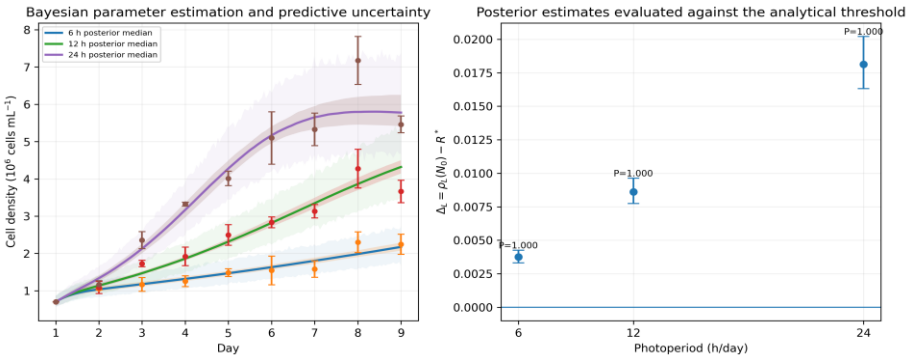


Figure 6 Connection between Bayesian parameter estimation and the analytical dynamical conditions. Left: observed biomass summaries together with trajectories implied by posterior parameter values. Right: the same posterior draws evaluated through $\Delta_L = \rho_L(N_0) - R^*$; positive values indicate that the estimated nutrient-uptake capacity exceeds the biomass-maintenance requirement.

We propagated posterior uncertainty through the ODEs to predict final biomass and biomass area under the curve (AUC). To identify which fitted parameters are associated with variation in each output, we calculated partial rank correlation coefficients (PRCC), controlling for the monotonic effects of the other estimated parameters. PRCC measures association rather than fit quality. Its magnitude indicates the strength of the conditional monotonic relationship, and its sign indicates direction.

The leading association depends on the photoperiod and the outcome. For final biomass, the largest absolute PRCC belonged to the effective light ratio at 6 h (0.475) but to N_0 at 12 h (0.570) and 24 h (0.997). For biomass AUC, the leading parameter was $Q(0)$ at 6 h (0.741), the light ratio at 12 h (0.445), and N_0 at 24 h (0.807). This pattern is consistent with the model mechanism: light response and initial quota matter more during shorter illumination, whereas the larger light input at 24 h makes available external nutrient the main source of variation in predicted biomass (Table 4).

Table 4 Dominant posterior parameter–output associations based on partial rank correlation coefficients (PRCC). For each photoperiod and output, the parameter with the largest |PRCC| is reported; magnitude indicates association strength and sign indicates direction after accounting for the other estimated parameters.

Photoperiod	Output	Dominant parameter	PRCC
6 h	final biomass	I_0/I_{opt}	0.475
12 h	final biomass	N_0	0.570
24 h	final biomass	N_0	0.997
6 h	biomass AUC	$Q(0)$	0.741
12 h	biomass AUC	I_0/I_{opt}	0.445
24 h	biomass AUC	N_0	0.807

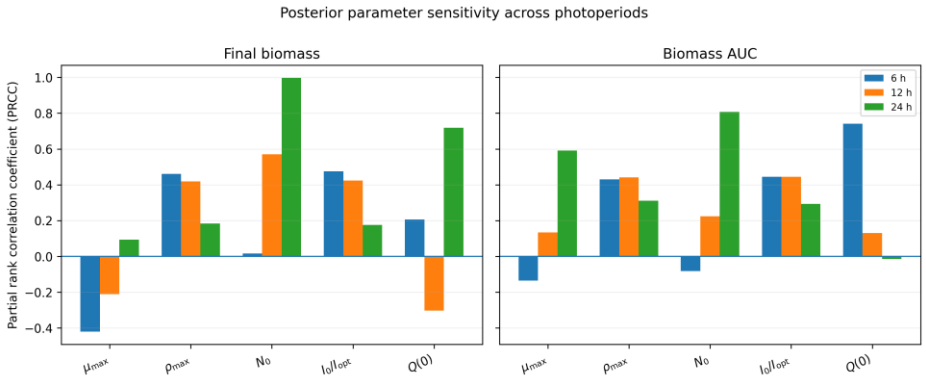


Figure 7 Posterior sensitivity profiles for final biomass and biomass AUC across photoperiods. Bars show signed PRCC values for all estimated parameters; larger |PRCC| indicates stronger association with predictive variation, while the sign indicates direction after accounting for the remaining parameters.

Figure 7 displays the signed PRCC values for all estimated parameters, so both the strength and direction of their association with predictive uncertainty can be compared across photoperiods.

8 Model Comparison and Practical Interpretation of Photoperiod

We fitted Logistic, Monod, and Droop–Steele models to the same 81 container-day observations and compared them on a common log-residual scale.

To clarify the benchmark specification, the Logistic model was used as a descriptive treatment-specific growth model, whereas the Monod model represented biomass growth as a direct function of external nutrient concentration without an internal-quota state; the Droop–Steele model retained the nutrient–quota–biomass structure described above. The parameter count k includes all fitted model parameters and the residual-scale parameter, giving k = 10 for Logistic and k = 6 for both Monod and Droop–Steele. For each model, the small-sample corrected Akaike information criterion was computed from the maximized log-likelihood on the same n = 81 log-scale observations as

$$\mathrm{AICc} = -2\ell_{max} + 2k + \frac{2k(k+1)}{n-k-1}.$$

The reported model differences were calculated relative to the minimum AICc:

$$\Delta\mathrm{AICc}_i = \mathrm{AICc}_i - \mathrm{AICc}_{min}.$$

Here, AICc_{min} denotes the smallest AICc among the compared models. Thus, log-RMSE summarizes unadjusted residual error, whereas AICc compares the fitted models after accounting for parameter count.

Logistic has a slightly smaller raw log-RMSE than Droop–Steele (0.1220 versus 0.1229), so the latter does not give the smallest unadjusted residual error. Droop–Steele nevertheless has the lowest AICc (-96.65), compared with -87.79 for Logistic and -77.04 for Monod, after accounting for parameter count. The respective ΔAICc values are 0, 8.85, and 19.61 (Table 5).

Table 5 Comparison on the same 81 container-day observations. The parameter count k includes the residual-scale parameter.

Model	k	log-RMSE	AICc	ΔAICc	Structural interpretation
Droop–Steele	6	0.1229	-96.65	0.00	nutrient + quota + light-mediated uptake
Logistic	10	0.1220	-87.79	8.85	descriptive treatment-specific growth curves
Monod	6	0.1387	-77.04	19.61	external nutrient, no internal quota

Figure 8 visualizes the corresponding ΔAICc values and annotates the raw log-RMSE, separating complexity-adjusted model support from residual error.

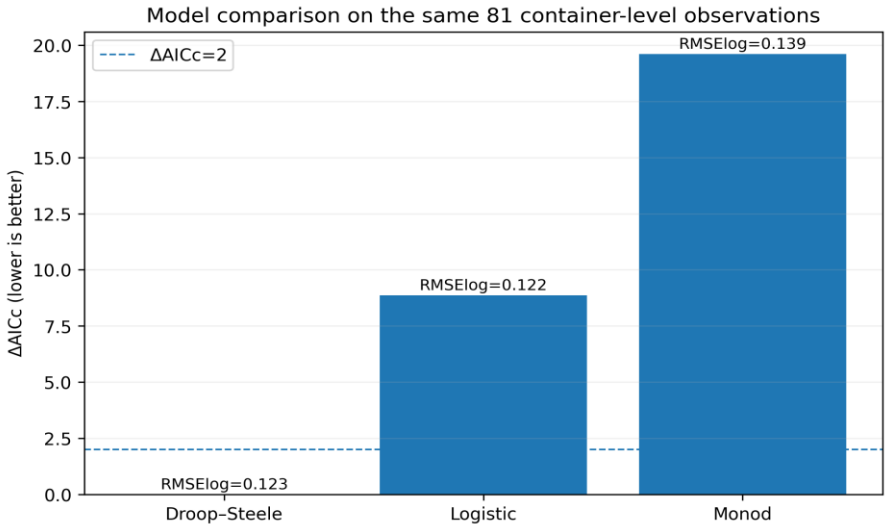


Figure 8 The comparison of ΔAICc for Logistic, Monod, and Droop–Steele models on the same 81 container-day observations. Raw log-RMSE values are annotated to distinguish fit error from complexity-adjusted evidence.

The three photoperiod treatments allow us to compare growth under controlled lighting conditions and to consider an initial operational implication. At the posterior medians, predicted final biomass rises from 2.17 at 6 h to 4.31 at 12 h and 5.79 at 24 h, in units of 10^6 cells ml^{-1}. Biomass AUC also rises, but AUC per lighting hour falls from 0.247 to 0.201 and then 0.161. Additional lighting therefore yields progressively less biomass benefit per hour. This biological trade-off could be combined with lamp power, electricity price, and other operating costs in a future economic optimization; the present data alone do not establish a cost-optimal photoperiod.

Because photoperiod enters the fitted model continuously through f_L, we can also examine durations between those tested experimentally. Figure 9 shows posterior-median day-9 predictions at 2-h increments from 6 h to 24 h. Predicted biomass rises from 2.17 to 5.79, with a gradually flattening curve. Values at intermediate durations are model predictions, not additional experimental measurements.

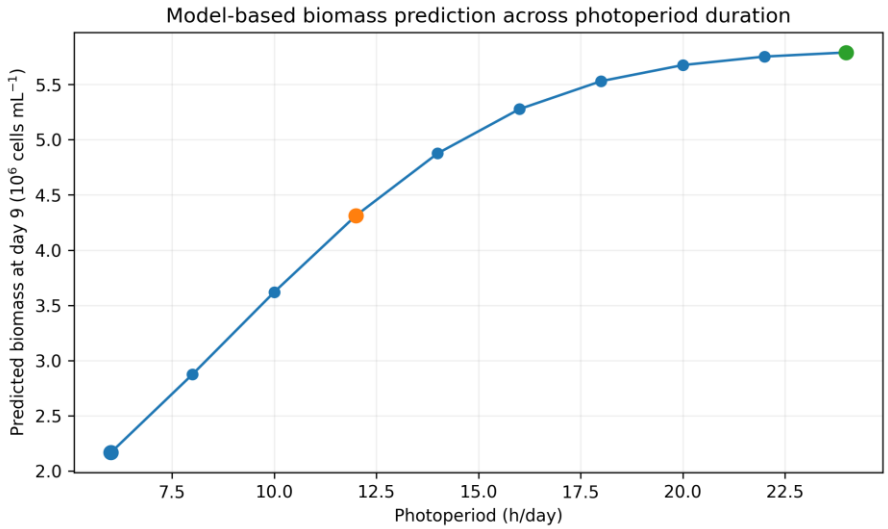


Figure 9 Model-based day-9 biomass prediction for intermediate photoperiod durations between the tested 6 h and 24 h treatments. The 6 h, 12 h, and 24 h values correspond to experimentally tested durations; the remaining values are predictions from the same estimated model.

8.1 Numerical Interpretation of the Estimated Steele Light Response

The posterior median for I_0/I_{opt} is 0.02578 (5–95%: 0.00679–0.07937; Table 3). In the effective-light model, $z = I_L/I_{\mathrm{opt}} = (L/24)\left(I_0/I_{\mathrm{opt}}\right)$ remains well below the Steele optimum of $z = 1$ for all tested photoperiods. At the median parameter values, z increases from 0.00645 at 6 h to 0.02578 at 24 h. The model therefore operates on the nearly linear, increasing part of the response. This does not establish the actual irradiance regime, which cannot be identified separately from biomass measurements.

Figure 10 provides a numerical check. At 6 h, 12 h, and 24 h, the posterior-median Steele factor differs from the low-light approximation $f_L \approx ez$ by just 0.65%, 1.30%, and 2.61%, respectively. Using this approximation changes predicted day-9 biomass by no more than 1.16% at the observed photoperiods, yet the biomass curve still flattens. The flattening is therefore not evidence, by itself, of Steele-type photoinhibition.

The predicted nutrient and quota trajectories offer an alternative explanation. At day 9, posterior-median external nutrient levels are 0.124, 0.052, and 0.00465 under 6 h, 12 h, and 24 h lighting. The corresponding saturation factors

$N/(K_N + N)$ decline from 0.293 to 0.148 and 0.015. At 24 h, quota also approaches its subsistence level: $Q(t_9) = 0.03025$ compared with $Q_0 = 0.03$. Longer illumination initially increases uptake, but nutrient depletion and low quota increasingly restrict the extra growth it can produce.

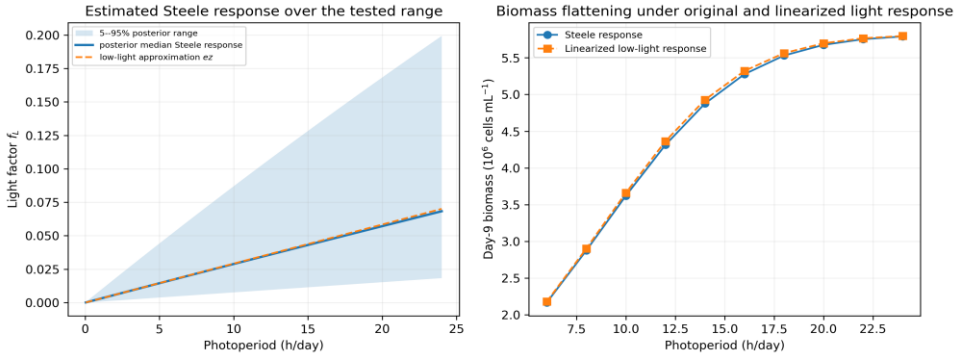


Figure 10 Numerical diagnostic of the estimated light-response regime. Left: Steele factor over 0–24 h with the 5–95% posterior range and posterior-median low-light approximation. Right: day-9 biomass predicted by the original Steele response and its linearized low-light approximation. Their close agreement shows that the predicted flattening over 6–24 h is consistent with nutrient–quota dynamics rather than requiring Steele-type photoinhibition.

The relation between the three model structures can be made more explicit. If the internal quota adjusts much faster than biomass, then $\dot{Q} \approx 0$ gives

$$Q \approx Q_0 + \frac{\rho_L(N)}{\mu_{\max}}. \tag{27}$$

Substitution of Eq. (27) into the Droop growth function yields

$$\mu(Q) \approx \frac{\mu_{\max}\rho_L(N)}{\mu_{\max}Q_0 + \rho_L(N)} = \mu_{M,L}\frac{N}{K_{M,L} + N}, \tag{28}$$

where

$$\mu_{M,L} = \frac{\mu_{\max}\rho_{\max}f_L}{\mu_{\max}Q_0 + \rho_{\max}f_L}, \qquad K_{M,L} = \frac{\mu_{\max}Q_0K_N}{\mu_{\max}Q_0 + \rho_{\max}f_L}. \tag{29}$$

Under a fast-quota approximation, the reduced growth law thus takes the Monod functional form, with effective parameters that vary with photoperiod. Retaining

Q as a separate state allows Droop–Steele to represent quota dynamics that this reduction removes.

The Logistic equation is not an exact parameter special case of the present system. It can be obtained only as a local phenomenological reduction after the nutrient and quota states are eliminated and the net per-capita growth rate is approximated by $g(X) \approx r - \beta X$, giving

$$\dot{X} \approx rX\left(1 - \frac{X}{K}\right), \qquad K = r/\beta.$$

Droop–Steele contains more physiological state information than the Logistic description, but Logistic is not an exact nested special case of the proposed system.

9 Discussion

The model comparison illustrates why fit and mechanism need to be considered separately. Logistic describes the observed curves with a marginally lower raw log-RMSE, but its treatment-specific parameters do not identify nutrient uptake or intracellular storage. Monod includes external nutrient but makes growth respond directly to it, without separating uptake from growth through quota. Droop–Steele provides that separation and has the lowest AICc in this comparison, while also yielding a light-dependent uptake pathway and a persistence threshold that can be analyzed mathematically. The fitted Steele response, however, remains on its nearly linear increasing branch over 6–24 h. These experiments do not establish photoinhibition: the diagnostic in Figure 10 instead shows that depletion of external nutrient and limitation by intracellular quota can account for the diminishing biomass gains predicted by the model.

For our question, the persistence threshold adds information that a carrying capacity cannot provide. Equation (19) links Δ_L both to the existence of positive biomass and to the sign of the biomass-direction eigenvalue at washout. At $\Delta_L = 0$, the equilibrium branches meet; numerical continuation displays the corresponding change in local stability. The boundedness argument and the numerical tests across initial conditions provide further context, although neither replaces a proof of global stability.

The Bayesian results can also be interpreted in dynamical terms rather than solely as parameter intervals. We calculate Δ_L and assess positive-equilibrium stability for each posterior draw. All three experimental treatments support persistence

within the fitted model and the estimated margin grows with lighting duration. The treatments therefore differ in predicted biomass more than in their qualitative equilibrium regime. This use of Bayesian inference builds on mechanistic bioprocess parameter-estimation approaches [23, 27], with the persistence margin providing an interpretable link between estimation and dynamics.

The uncertainty analysis points to measurements that could make future experiments more informative. A parameter with a broad posterior is not necessarily the largest contributor to uncertainty in each output. At 24 h, N_0 has the strongest association with final-biomass variation; at 6 h, the effective light ratio is more influential. Measuring nutrient concentrations would therefore be particularly helpful for predictions under long photoperiods, while direct irradiance and uptake measurements would help at shorter durations. Such measurements could also reduce the observed confounding between $\rho_{\max}$ and I_0/I_{opt}.

Several limitations affect how far these findings can be taken. We replaced the daily light/dark cycle with one effective light factor, so the model cannot resolve within-day switching, night-time physiology, or recovery from photoinhibition; those questions require time-resolved light and metabolic data [28]. Irradiance was not measured independently and the fitted effective response does not provide empirical evidence for or against photoinhibition. Each treatment had only three independent cultures. Observations from the same container may be temporally correlated, whereas the likelihood assumes independent log-scale errors; the reported posterior uncertainty is conditional on that assumption. We used microscopic cell density as a biomass proxy and fix several physiological parameters because cell-density data alone do not identify them all. The parameter-perturbation and initial-condition tests cover finite ranges and do not prove global stability. A formal center-manifold bifurcation result is also beyond the present analysis. Finally, AUC per lighting hour is a biological measure, not a financial one: a cost-based optimum would require electricity use, pricing, and other operating expenses.

10 Conclusion

We developed a Droop–Steele model for *Porphyridium* sp. cultures exposed to 6 h, 12 h, and 24 h photoperiods and studied it using mathematical analysis, numerical simulations, and Bayesian estimation. The biologically feasible region is forward invariant, and the solutions are ultimately bounded. We derived a washout–persistence threshold, showed how it determines the biomass-direction eigenvalue at washout and obtained a Routh–Hurwitz condition for local stability

of the positive equilibrium. Numerical continuation and tests from multiple initial conditions were consistent with this local stability analysis.

The model was fitted to 81 container-day observations and the four Bayesian chains met the prespecified convergence criteria. Applying the analytical conditions to posterior draws gave persistence and positive-equilibrium local-stability proportions of 1.000 for each tested photoperiod, with larger persistence margins under longer illumination. The dominant sources of predictive uncertainty varied with photoperiod. Droop–Steele had the lowest AICc among the three models compared, although Logistic had a marginally lower raw log-RMSE. More hours of light increased predicted biomass but reduced biomass AUC per lighting hour. Importantly, the fitted effective Steele response remained nearly linear: the flattening in predicted biomass is consistent with nutrient depletion and quota limitation, not evidence of photoinhibition. Future work should measure irradiance and nutrient concentrations directly and combine the biological predictions with energy and operating-cost data before recommending a cost-optimal lighting schedule.

Data and Code Availability

The experimental data and computational code supporting the findings of this study are available from the corresponding author upon reasonable request.

Acknowledgement

The authors thank the staff of Balai Besar Perikanan Budidaya Laut (BBPBL) Lampung for providing culture facilities and supporting the *Porphyridium* sp. photoperiod experiments that motivated this study.

Nomenclature

N	**external limiting nutrient**
X	biomass proxy or cell density
Q	internal quota
D	effective nutrient refresh or dilution rate
N_0	reference external nutrient concentration
m	biomass loss rate
$\mu_{\max}$	maximum specific growth rate

Q_0	subsistence quota
$\rho_{\max}$	maximum uptake rate
K_N	half-saturation nutrient level
I_0/I_{opt}	effective light ratio
L	photoperiod duration
Δ_L	persistence margin $\rho_L(N_0) - R^*$

References

[1] Alyaniazy, S., Tiyas, P.R., Ma'arif, N.I. & Sari, A.N., *Teknik Kultur Fitoplankton Chlorella vulgaris sebagai Pakan Alami Ikan Kerapu Cantang*, JFMR (Journal of Fisheries and Marine Research), **7**(3), pp. 89-96, 2023. DOI: 10.21776/ub.jfmr.2023.007.03.10.

[2] Al Adawiyah, L., Ulkhaq, M.F. & Kenconojati, H., *Growth Response of Porphyridium sp. Culture on Glass and Plastic Container in Laboratory Scale*, Journal of Aquaculture and Fish Health, **9**(2), pp. 155-163, 2020. DOI: 10.20473/jafh.v9i2.17183.

[3] Syaifudin, M.S., Sulmartiwi, L. & Andriyono, S., *Penambahan Mikroalga Merah Porphyridium cruentum pada Pakan Terhadap Kecerahan Warna Ikan Cupang (Betta splendens)*, Journal of Aquaculture and Fish Health, **6**(1), pp. 41-47, 2017. DOI: 10.20473/jafh.v6i1.11274.

[4] Rafaelina, M., Rustam, Y. & Amini, S., *Pertumbuhan dan Aktivitas Antioksidan dari Mikroalga*, Bioma, **11**(1), pp. 12-21, 2015. DOI: 10.21009/Bioma11(1).2.

[5] Sosa-Hernandez, J.E., Rodas-Zuluaga, L.I., Castillo-Zacarias, C., et al., *Light Intensity and Nitrogen Concentration Impact on the Biomass and Phycoerythrin Production by Porphyridium purpureum*, Marine Drugs, **17**(8), 460, 2019. DOI: 10.3390/md17080460.

[6] Kim, S.H., Lee, U.H., Lee, S.B., Jeong, G.T. & Kim, S.K., *Improvement of Unsaturated Fatty Acid Production from Porphyridium cruentum Using A Two-phase Culture System in A Photobioreactor with Light-emitting Diodes (LEDs)*, Journal of Microbiology and Biotechnology, **31**(3), pp. 456-463, 2021. DOI: 10.4014/jmb.2011.11004.

[7] Liberti, D., Imbimbo, P., Giustino, E., et al., *Inside Out Porphyridium cruentum: Beyond the Conventional Biorefinery Concept*, ACS Sustainable Chemistry & Engineering, **11**(1), pp. 381-389, 2023. DOI: 10.1021/acssuschemeng.2c05869.

[8] Casas-Arrojo, V., Decara, J., Arrojo-Agudo, M.A., Pérez-Manríquez, C. & Abdala-Díaz, R.T., *Immunomodulatory, Antioxidant Activity and*

Cytotoxic Effect of Sulfated Polysaccharides from Porphyridium cruentum (S.F.Gray) Nägeli, Biomolecules, **11**(4), 488, 2021. DOI: 10.3390/biom11040488.

[9] Li, C., Wu, H., Wu, H., Xiang, W., Xu, J. & Li, T., *Enhancing Phycoerythrin Production of Marine Red Microalga Porphyridium Purpureum with Low Salinity and Semi-continuous Culture Strategy*, Marine Drugs, **23**(9), 361, 2025. DOI: 10.3390/md23090361.

[10] Droop, M.R., *Vitamin B12 and Marine Ecology. IV. The Kinetics of Uptake, Growth and Inhibition in Monochrysis lutheri*, Journal of the Marine Biological Association of the United Kingdom, **48**(3), pp. 689-733, 1968. DOI: 10.1017/s0025315400019238.

[11] Droop, M.R., *Some Thoughts on Nutrient Limitation in Algae*, Journal of Phycology, **9**(3), pp. 264-272, 1973. DOI: 10.1111/j.1529-8817.1973.tb04092.x.

[12] Saccardo, A., Felices-Rando, B., Sforza, E. & Bezzo, F., *Droop Model Identification Via Model-based Design of Experiments to Describe Microalgae Nitrogen Uptake in Continuous Photobioreactors*, Chemical Engineering Journal, **468**, 143577, 2023. DOI: 10.1016/j.cej.2023.143577.

[13] Martínez, C., Mairet, F. & Bernard, O., *Dynamics of the Periodically Forced Light-limited Droop Model*, Journal of Differential Equations, **269**(4), pp. 3890-3913, 2020. DOI: 10.1016/j.jde.2020.03.020.

[14] Alzahrani, E.O., El-Dessoky, M.M. & Dogra, P., *Global Dynamics of A Cell Quota-based Model of Light-dependent Algae Growth in A Chemostat*, Communications in Nonlinear Science and Numerical Simulation, **90**, 105295, 2020. DOI: 10.1016/j.cnsns.2020.105295.

[15] Baroukh, C., Mairet, F. & Bernard, O., *The Paradoxes Hidden Behind the Droop Model Highlighted by A Metabolic Approach*, Frontiers in Plant Science, **13**, 941230, 2022. DOI: 10.3389/fpls.2022.941230.

[16] Molina-Miras, A., Bueso-Sánchez, A., Cerón-García, M.C., Sánchez-Mirón, A., Contreras-Gómez, A. & García-Camacho, F., *Effect of Nitrogen, Phosphorous, and Light Colimitation on Amphidinol Production and Growth in the Marine Dinoflagellate Microalga Amphidinium carterae*, Toxins, **14**(9), 594, 2022. DOI: 10.3390/toxins14090594.

[17] Mairet, F. & Baron, R., *A Physiologically Structured Equation to Consider Quota Heterogeneity in the Droop Model*, IFAC-PapersOnLine, **52**(26), pp. 275-280, 2019. DOI: 10.1016/j.ifacol.2019.12.270.

[18] Shoener, B.D., Schramm, S.M., Beline, F., Bernard, O., Martinez, C., Plosz, B.G., Snowling, S., Steyer, J.-P., Valverde-Perez, B., Wagner, D. & Guest, J.S., *Microalgae and Cyanobacteria Modeling in Water Resource Recovery Facilities: A Critical Review*, Water Research X, **2**, 100024, 2019. DOI: 10.1016/j.wroa.2018.100024.

[19] Monod, J., *The Growth of Bacterial Cultures*, Annual Review of Microbiology, **3**(1), pp. 371-394, 1949. DOI: 10.1146/annurev.mi.03.100149.002103.

[20] Lemesle, V. & Mailleret, L., *A Mechanistic Investigation of the Algae Growth "Droop" Model*, Acta Biotheoretica, **56**(1-2), pp. 87-102, 2008. DOI: 10.1007/s10441-008-9031-3.

[21] Steele, J.H., *Environmental Control of Photosynthesis in the Sea*, Limnology and Oceanography, **7**(2), pp. 137-150, 1962. DOI: 10.4319/lo.1962.7.2.0137.

[22] Smith, H.L. & Waltman, P., *The Theory of the Chemostat: Dynamics of Microbial Competition*, Cambridge University Press, Cambridge, 5-10, 1995. DOI: 10.1017/cbo9780511530043.

[23] Helleckes, L.M., Osthege, M., Wiechert, W., von Lieres, E. & Oldiges, M., *Bayesian Calibration, Process Modeling and Uncertainty Quantification in Biotechnology*, PLOS Computational Biology, **18**(3), e1009223, 2022. DOI: 10.1371/journal.pcbi.1009223.

[24] Tonner, P.D., Darnell, C.L., Bushell, F.M.L., Lund, P.A., Schmid, A.K. & Schmidler, S.C., *A Bayesian Non-parametric Mixed-effects Model of Microbial Growth Curves*, PLOS Computational Biology, **16**(10), e1008366, 2020. DOI: 10.1371/journal.pcbi.1008366.

[25] Puspita, D., Nadia, N., Wijaya, M., Fauzi, R. & Soewono, E., *A Semi-analytic Prediction of Reserve Under Pandemic Risk: COVID-19 in Indonesia As A Case Study*, Scandinavian Actuarial Journal, pp. 1-25, 2026. DOI: 10.1080/03461238.2026.2673558.

[26] Oh, S.H., Han, J.G., Kim, Y., Ha, J.H., Kim, S.S., Jeong, M.H., Jeong, H.S., Kim, N.Y., Cho, J.S., Yoon, W.B., Lee, S.Y., Kang, D.H. & Lee, H.Y., *Lipid Production in Porphyridium cruentum Grown Under Different Culture Conditions*, Journal of Bioscience and Bioengineering, **108**(5), pp. 429-434, 2009. DOI: 10.1016/j.jbiosc.2009.05.020.

[27] Rosenbaum, B., Raatz, M., Weithoff, G., Fussmann, G.F. & Gaedke, U., *Estimating Parameters from Multiple Time Series of Population Dynamics Using Bayesian Inference*, Frontiers in Ecology and Evolution, **6**, 234, 2019. DOI: 10.3389/fevo.2018.00234.

[28] Gao, Y., Bernard, O., Fanesi, A., Perré, P. & Lopes, F., *The Impact of Light/dark Regimes on Structure and Physiology of Chlorella vulgaris Biofilms*, Frontiers in Microbiology, **14**, 1250866, 2023. DOI: 10.3389/fmicb.2023.1250866.